University of Groningen

Identification and characterization of archaeal and bacterial F420-dependent thioredoxin reductases

Yang, Guang; Wijma, Hein J; Rozeboom, Henriëtte J; Mascotti, Maria Laura; Fraaije, Marco W

Link to publication in University of Groningen/UMCG research database

Identification and characterization of archaeal and bacterial F$_{420}$-dependent thioredoxin reductases

Guang Yang[1], Hein J. Wijma[1], Henriëtte J. Rozeboom[1], Maria Laura Mascotti[1,2] (iD) and Marco W. Fraaije[1] (iD)

1 Molecular Enzymology Group, University of Groningen, The Netherlands
2 IMIBIO-SL CONICET, Facultad de Química Bioquímica y Farmacia, Universidad Nacional de San Luis, Argentina

The thioredoxin pathway is an antioxidant system present in most organisms. Electrons flow from a thioredoxin reductase to thioredoxin at the expense of a specific electron donor. Most known thioredoxin reductases rely on NADPH as a reducing cofactor. Yet, in 2016, a new type of thioredoxin reductase was discovered in Archaea which utilize instead a reduced deazaflavin cofactor (F$_{420}$H$_2$). For this reason, the respective enzyme was named deazaflavin-dependent flavin-containing thioredoxin reductase (DFTR). To have a broader understanding of the biochemistry of DFTRs, we identified and characterized two other archaeal representatives. A detailed kinetic study, which included pre-steady state kinetic analyses, revealed that these two DFTRs are highly specific for F$_{420}$H$_2$ while displaying marginal activity with NADPH. Nevertheless, they share mechanistic features with the canonical thioredoxin reductases that are dependent on NADPH (NTRs). A detailed structural analysis led to the identification of two key residues that tune cofactor specificity of DFTRs. This allowed us to propose a DFTR-specific sequence motif that enabled for the first time the identification and experimental characterization of a bacterial DFTR.

Introduction

F$_{420}$ is a deazaflavin cofactor that was discovered in 1970 [1]. For several decades, it was considered to be only distributed in methanogens [2], hydrogenotrophs [2–4], and some specific actinobacteria [5–9]. However, F$_{420}$ has been found in many more microorganisms [10–13]. In methanogens, F$_{420}$ serves as a redox cofactor and is required by enzymes involved in the CO$_2$-reducing pathway to produce methane [2,10,14–18]. In bacteria, the deazaflavin cofactor and its related enzymes were found to be crucial for dealing with oxidative stress, nitrosative stress, and activating antibacterial prodrugs [10,19–22]. F$_{420}$ is also required by

some streptomycetes for the synthesis of antibiotics [23–27].

The F$_{420}$ cofactor contains a 5-deaza-isoalloxazine moiety which is structurally similar to the redox-active part of the canonical flavin cofactors, FAD and FMN (Fig. 1A,B). It has a maximum absorbance of 420 nm, hence its name [2]. One main difference between F$_{420}$ and flavin cofactors is that the nitrogen atom at position 5 of the isoalloxazine ring in flavins is substituted by a carbon atom. Furthermore, the natural flavin cofactors have two methyl groups at the C7 and C8 positions, while F$_{420}$ has a hydroxyl group at C8 and

no substituent at C7. Those differences cause F$_{420}$ to have a relatively low redox potential (−340 mV), which is not only lower than those of flavins (−220 mV) but also nicotinamides (−320 mV) [28,29]. In addition, because of the substitution of N5 for a carbon atom, F$_{420}$ can only catalyze hydride transfer reactions similar to nicotinamide cofactors [30,31]. In fact, F$_{420}$ can be regarded as a decorated nicotinamide cofactor: its 5-deaza-isoalloxazine part contains a nicotinamide moiety (Fig. 1B,C).

Until recently, only a few F$_{420}$-dependent enzymes had been extensively investigated. However, they have attracted more attention recently because of their potential use in tuberculosis treatment, methane mitigation, bioremediation, and industrial biocatalysis [10,32]. In 2016, a novel F$_{420}$H$_2$-dependent enzyme was discovered in a strictly anaerobic methanogenic archaeon, *Methanocaldococcus jannaschii* [33]. This enzyme was found to have the highest sequence identity to FAD-containing NADPH-dependent thioredoxin reductases (NTRs) [34]. Indeed, like previously studied NTRs, it was found to contain a tightly bound FAD cofactor and two cysteines as redox center close to the flavin cofactor. The most significant difference with NTR is that the enzyme uses F$_{420}$H$_2$, instead of NADPH, as its electron donor to reduce thioredoxin (Trx). Therefore, it was named deazaflavin-dependent flavin-containing thioredoxin reductase (DFTR). As a thioredoxin reductase, DFTR together with endogenous thioredoxins and reduced F$_{420}$ forms a functional thioredoxin pathway in anaerobic methanogens [33,34]. Thioredoxins are small proteins of around 12 kDa that contain two redox-active cysteines that can form an intermolecular disulfide bond. This disulfide bond is reduced by TR upon which the reduced Trx can interact with a plethora of other proteins involved in biological processes such as antioxidant processes, redox regulation, and enzyme activation (Fig. 2) [35].

The above-mentioned study was so far the only report on a thioredoxin reductase that uses F$_{420}$ as an electron donor. This motivated us to identify and study other DFTRs which may help in improving our understanding of the multiple roles of F$_{420}$ in enzymes. We identified two other DFTRs and investigated their biochemical properties. These are named *Ma*-DFTR and *Mv*-DFTR according to their origin: *Methanococcus aeolicus* and *Methanococcus voltae* (WP_013180053.1 and WP_011973481.1, respectively). The newly identified DFTRs have moderate sequence identities with the first reported DFTR (*Mj*-DFTR): 64% and 55% for *Ma*-DFTR and *Mv*-DFTR, respectively. They share much lower sequence identities with the NTR from *Escherichia coli*: 36% and 27%, respectively. The sequence identity among the two new DFTRs is 52%. Furthermore, several endogenous thioredoxins were identified and used as recombinant proteins in this study: *Ma*-Trx2 (WP_011973221.1), *Ma*-Trx3 (WP_011973049.1), *Mv*-Trx1 (WP_013180636.1), and *Mv*-Trx2 (WP_013180369.1). Both *Ma*-DFTR and *Mv*-DFTR were found to catalyze
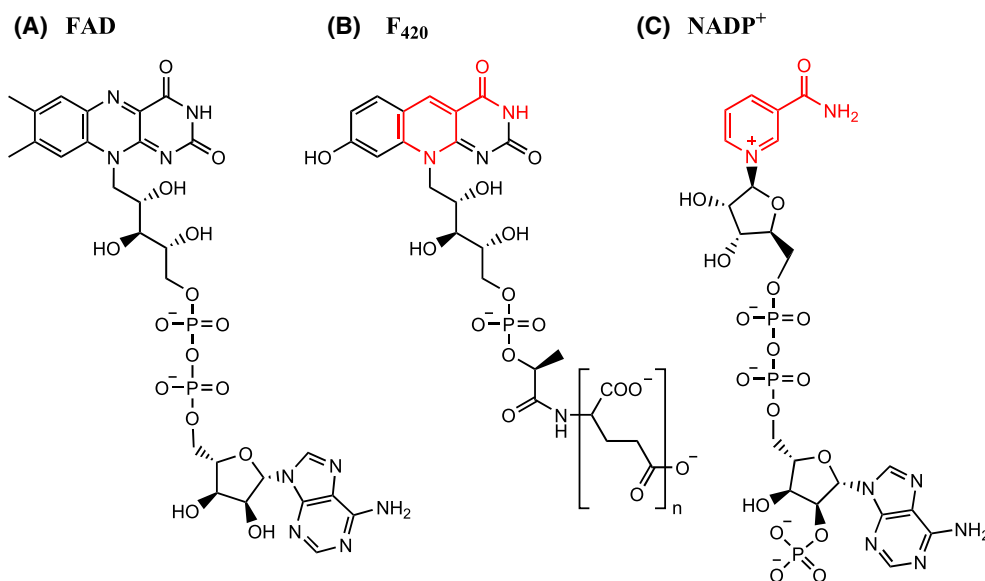
Fig. 1. Redox cofactors investigated in this work: FAD (A), F$_{420}$ (B), and NADP$^+$ (C). The structure highlighted in red is the nicotinamide portion in F$_{420}$ and NADP$^+$.
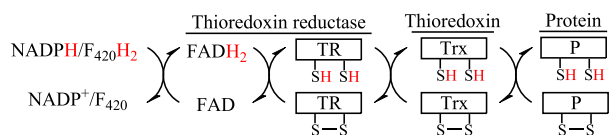
Fig. 2. Electron flow in NADPH/F$_{420}$-dependent thioredoxin reductases.

the reduction of the corresponding thioredoxins using F$_{420}$H$_2$. AlphaFold models were generated, analyzed and a specific DFTR motif was proposed. This motif led us to successfully discover a DFTR from a bacterium, the aerobic actinomycete *Longimycelium tulufanense*. Our research shows that DFTRs are more widespread in nature than originally conceived, suggesting a broader role of F$_{420}$ in biology.

Results

Expression, purification, and hydrodynamic properties

Ma-DFTR and *Mv*-DFTR were expressed as N-terminal His-tagged SUMO fusion proteins in *E. coli* NEB 10-β cells. All the selected thioredoxins were also expressed as N-terminal His-tagged proteins. Both DFTRs were purified with high yields as soluble yellow-colored proteins (*Ma*-DFTR: 100–120 mg·L^{-1}; *Mv*-DFTR: 50–60 mg·L^{-1}) (Fig. S1). The four thioredoxins could be expressed and purified as soluble proteins as well, albeit with lower yields (20–50 mg·L^{-1}) (Fig. S1). The UV–vis absorbance spectra of the DFTRs revealed two specific absorbance maxima at 370 and 450 nm indicative of the presence of a flavin cofactor (Fig. S2). In fact, the intense yellow color of the purified proteins was already a clear indication that they contain a tightly bound flavin cofactor.

For determining the oligomeric state of the DFTRs, the SUMO-tag was removed and size exclusion chromatography (SEC) and dynamic light scattering (DLS) analyses were performed. SEC analysis of *Ma*-DFTR showed two main peaks with one in the void volume of the column, indicating aggregation of the protein, and one corresponding to a molecular mass of 78 kDa. DLS analysis of protein obtained by SEC did not result in a stable signal, suggesting re-aggregation after SEC. Upon SEC, the *Mv*-DFTR eluted mainly in one peak that corresponds to a protein of 82 kDa. DLS analysis of the SEC-purified *Mv*-DFTR sample showed 17% polydispersity and no high molecular mass aggregates (data not shown). The observed hydrodynamic radius of 3.44 nm corresponds to a

molecular mass of 61 kDa. These results indicate that *Mv*-DFTR is dimeric in solution, similar to NTRs.

The thermostability of *Ma*-DFTR and *Mv*-DFTR was determined by measuring their melting temperatures (T_m) using ThermoFAD [36] and Thermofluor [37]. The two different methods resulted in the same T_m values for each DFTR. *Ma*-DFTR and *Mv*-DFTR are thermostable at pH 8.0 with apparent T_m values of 89 °C and 76 °C, respectively (Fig. S3). This is fortuitous since both archaea are mesophilic.

Steady-state kinetics

In the first kinetic experiments, it was observed that F$_{420}$H$_2$ was consumed in the absence of any disulfide substrate, such as DNTB (5,5′-dithiobis(2-nitrobenzoic acid)) or thioredoxin. This suggested that oxygen can act as an electron acceptor, thereby forming hydrogen peroxide and/or superoxide as a product. It is known that flavoenzymes, in the reduced state, can indeed funnel electrons to dioxygen, often referred to as uncoupling activity. To investigate the uncoupling activities, an assay based on horseradish peroxidase (HRP) was used to detect hydrogen peroxide formation. No significant amounts of hydrogen peroxide could be detected in the first 10 min when the enzymes were incubated with F$_{420}$H$_2$. Only when the assay was monitored for > 60 min, formation of significant amounts of hydrogen peroxide observed. This hinted to the formation of superoxide which spontaneously disproportionates into hydrogen peroxide [38]. To confirm that the superoxide is an uncoupling product of the DFTRs, the cytochrome *c* reduction assay was used. In this assay, cytochrome *c* is reduced by superoxide causing a significant change of absorbance at 550 nm. These measurements confirmed that both archaeal DFTRs catalyze F$_{420}$H$_2$-fueled formation of superoxide when used in aerobic conditions at a rate of 0.027 s^{-1}. Interestingly, we found that cytochrome *c* can also be reduced when incubated with F$_{420}$H$_2$ in the absence of a DFTR. Yet, this was significantly slower: 0.006 s^{-1}. This confirms that superoxide is produced in aerobic conditions as uncoupling product. It shows that the archaeal DFTRs are a potential source of harmful reactive oxygen species (ROS). Such ROS generation ability is not biologically relevant as methanogens are strict anaerobes. Yet, for all subsequent experiments, anoxic conditions were used to eliminate any influence of dioxygen as a potential electron acceptor.

The two archaeal DFTRs were found to be able to reduce the artificial electron acceptor DTNB to TNB (5-thio-2-nitrobenzoic acid). This activity is a property

shared with NADPH-dependent thioredoxin reductases [39–41]. Intriguingly, both F$_{420}$H$_2$ and NADPH were accepted as electron donors by both enzymes. To determine the coenzyme preference, steady-state kinetic analyses were performed. A fixed DTNB concentration (1.0 mM) was used to perform the assays at 25 °C, pH 8.0 while varying the concentration of F$_{420}$H$_2$ (0–140 μM) and NADPH (0–800 μM). Interestingly, NADPH and F$_{420}$H$_2$ are accepted by both DFTRs. However, apparent K_m values of Ma-DFTR and Mv-DFTR for F$_{420}$H$_2$ were lower when compared with the K_m values for NADPH (Table 1). Additionally, the k_{cat} values for Ma-DFTR and Mv-DFTR with F$_{420}$H$_2$ (~ 3 s^{-1}) are two orders of magnitude higher than those with NADPH (~ 0.03 s^{-1}). The kinetic parameters with F$_{420}$ as coenzyme compared to those with NADPH suggest that these thioredoxin reductases are bona fide F$_{420}$-dependent enzymes.

To determine whether the selected thioredoxins are accepted as substrate by each corresponding DFTR, steady-state kinetics experiments were performed. The results revealed that all four thioredoxins can be reduced by the corresponding enzyme. The apparent K_m values of the corresponding enzymes for Ma-Trx2, Ma-Trx3, Mv-Trx1, and Mv-Trx2 are 2.4 ± 0.3 μM, 1.9 ± 0.2 μM, 4.4 ± 0.6 μM, and 1.1 ± 0.3 μM (Fig. 3). Mv-DFTR suffered from severe substrate inhibition with Mv-Trx2 as substrate, with a K_i of 4.7 ± 1.1 μM. These relatively low K_m values confirm that Ma-DFTR and Mv-DFTR are indeed thioredoxin reductases. Besides, in the insulin reduction assay, insulin could be reduced by all four thioredoxins in the presence of DFTRs and F$_{420}$H$_2$.

Given the relatively high thermostabilities of the two archaeal DFTRs, the effect of temperature on the activities was evaluated. Using a stopped-flow instrument, the activities were determined between 20 °C and 50 °C employing either Ma-Trx2 or Mv-Trx1 as substrates (Fig. S4). Going from 20 °C to 50 °C, the

activity increased about four-fold. Also, the effect of pH on activity was investigated. The activities decreased significantly at low pH values (pH < 5) for both DFTRs and they reached the highest activity between pH 6.0 and pH 8.0 (Fig. 4).
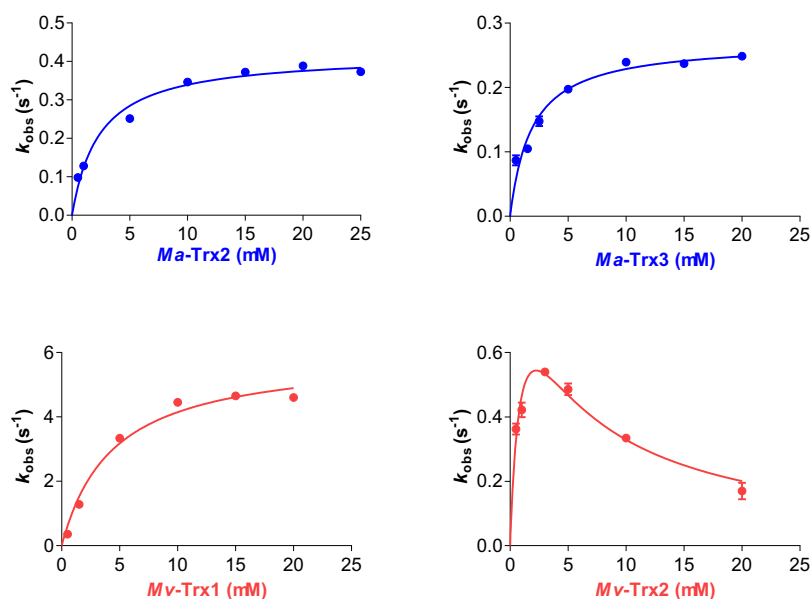
Pre-steady state kinetics

To investigate the catalytic mechanism of the two archaeal DFTRs in more detail, stopped-flow measurements were performed to analyze the reductive half-reactions. For this, the experiments were conducted in the absence of thioredoxin or any other potential electron acceptor. The measurements were performed using different F$_{420}$H$_2$ concentrations (2.5–75 μM) with a fixed enzyme concentration (5 or 10 μM) at 10 °C. The reduction of the DFTRs could be monitored by using the diode-array absorbance detection mode of the stopped-flow instrument. The spectral data obtained in reductive half-reactions with F$_{420}$H$_2$ could best be fitted to a two-step kinetic model in which two steps occur (Fig. 5 and Fig. S5). Based on the associated spectral features of the deconvoluted absorbance spectra, the first kinetic event mainly involves formation of oxidized F$_{420}$ (increase at 420 nm), where electrons are used to reduce the FAD (absorbance decrease at 450 nm). The rates of the initial kinetic process resulting in flavin reduction were found to be almost constant at different F$_{420}$H$_2$ concentrations suggesting that the K_d value for the coenzyme is lower than the lowest F$_{420}$H$_2$ concentration used (2.5 μM). For Mv-DFTR, the rate of flavin reduction was around 32.2 s^{-1} which is higher than that of Ma-DFTR (5.3 s^{-1}) (Table S1). In the second process, reduced FAD transfers electrons to reduce the active site disulfide, and the FAD then gets reduced again by F$_{420}$H$_2$ (continued increase of absorbance at 420 nm), resulting in two reduced active site cysteines and a reduced FAD cofactor. The rates for this step range

Table 1. Steady-state kinetic parameters of Ma-DFTR and Mv-DFTR for F$_{420}$H$_2$ and NADPH using DTNB as substrate. All measurements were conducted using a stopped-flow apparatus under anaerobic conditions at 25 °C in triplicate. The k_{obs} values were obtained from the initial rates of absorbance change at 400 nm.

| Enzymes | F$_{420}$H$_2$ | | | NADPH | | |
	k_{cat} (s^{-1})	K_m (μM)	k_{cat}/K_m (s^{-1}·mM^{-1})	k_{cat} (s^{-1})	K_m (μM)	k_{cat}/K_m (s^{-1}·mM^{-1})
Ma-DFTR	3.4 ± 2.3	343 ± 311	9.9	0.014 ± 0.001	434 ± 47	0.032
Mv-DFTR	2.4 ± 0.3	22.2 ± 6.7	110	0.029 ± 0.002	1580 ± 163	0.018
Mj-DFTR[a]	16[c]	28.6 ± 2.5	560	–	–	–
Ec-NTR[b]	–	–	–	23	3.0	7700

[a]Data are from previous work [33]; [b]Data are from previous work [64]; [c]The accurate k_{cat} value is not available in reference [33]. An estimated value based on the reported Michaelis–Menten curve is around 16 s^{-1}.

Fig. 3. Steady-state kinetic parameters of *Ma*-DFTR and *Mv*-DFTR toward the thioredoxins. All measurements were conducted using a stopped-flow apparatus under anaerobic conditions at 25 °C in triplicate. The k_{obs} values were obtained from the initial rates of absorbance change at 400 nm. Error bars indicate standard deviation values.
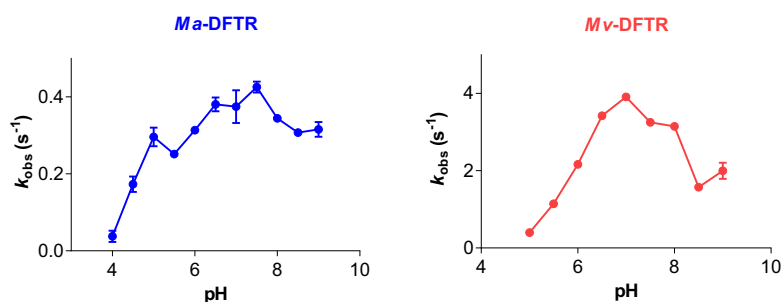
Fig. 4. pH optima for *Ma*-DFTR and *Mv*-DFTR. All measurements were conducted using a stopped-flow apparatus under anaerobic conditions at 25 °C in triplicate. The k_{obs} values were obtained from the initial rates of absorbance change at 400 nm. Error bars indicate standard deviation values.

from 0.15 to 0.6 s^{-1} for *Ma*-DFTR and 4.5 to 6.5 s^{-1} for *Mv*-DFTR relatively (Table S1). To confirm the nature of this second process, mutants of *Ma*-DFTR and *Mv*-DFTR were prepared which have two alanines instead of the two predicted active site cysteines (C130A/C133A-*Ma*-DFTR and C146A/C149A-*Mv*-DFTR). In these double mutants, the reduced FAD cannot shuttle electrons to the active site cysteines. As a result, the second equivalent of F$_{420}$H$_2$ would not be consumed. Indeed, when performing reductive half-reactions with the generated variants, the F$_{420}$H$_2$ consumption of the mutants was just half when compared with the wild-type enzymes. This confirms that the mutated cysteines are analogous to the redox-active cysteines found in the active site of NTRs.

Finally, when using 200 μM NADPH as electron donor, the observed rates of flavin reduction were only 0.054 ± 0.004 s^{-1} for *Ma*-DFTR and 0.029 ± 0.001 s^{-1} for *Mv*-DFTR. Clearly, the two DFTRs react much slower with the nicotinamide coenzyme compared with the deazaflavin coenzyme.

Structural analysis and modeling of coenzyme binding

As attempts to crystallize the two archaeal DFTRs failed, the three-dimensional structures of *Ma*-DFTR and *Mv*-DFTR were predicted using AlphaFold2 [42] (Fig. S6). The experimental structures of homologous FAD-containing NTRs exist in two conformations, of
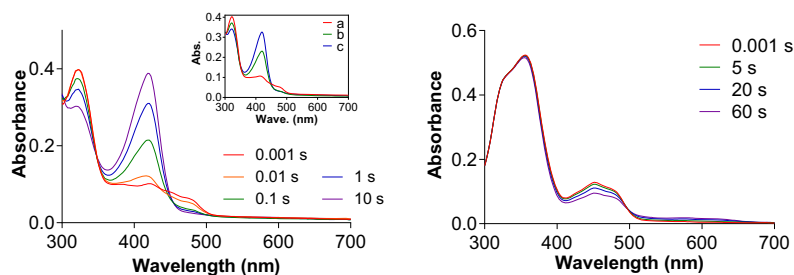
Fig. 5. Reductive half-reaction of *Mv*-DFTR. The reactions were conducted in a stopped-flow apparatus equipped with a photodiode array module in triplicate. The left panel shows the spectra of 5 μM *Mv*-DFTR mixed with 50 μM F$_{420}$H$_2$, while the right panel shows the spectra of 10 μM *Mv*-DFTR mixed with 200 μM NADPH. The insert in the left panel shows the deconvoluted spectra fitted into a two-step process a → b → c, yielding the corresponding fitted k_1 and k_2 rates, respectively.

which the Flavin Reducing (FR) conformation allows NADPH binding close to the flavin such that hydride transfer can occur [43]. Fortuitously, the fully automatic procedure predicted the FR structures for both DFTRs. The FAD binding orientation was obtained by superimposing the structural models to the NTR from *Lactococcus lactis* (see below). F$_{420}$, with a two-residue glutamyl tail, was hand-docked into the predicted structure. The resulting binding mode for the F$_{420}$ cofactor had an H-bonding pattern comparable to that of other F$_{420}$-containing proteins [44–48].

Two crystal structures of NTRs in an FR conformation were available [43,49] that allowed to make comparisons. These NTRs, from *E. coli* (*Ec*-NTR, PDB: 1F6M, 2.95 Å resolution) and *L. lactis* (*Ll*-NTR, PDB: 5MH4, 2.14 Å), share 34% sequence identity with each other. This is comparable to their sequence identities with the DFTRs (*Ll*-NTR to *Ma*-DFTR, 32%; *Ll*- NTR to *Mv*-DFTR, 31%; *Ec*-NTR to *Ma*-DFTR, 35%, *Ec*-NTR to *Mv*-DFTR, 25%). Visual inspection of them and the generated models revealed that the FAD binding site is not significantly different in the DFTRs.

The structures reveal some interesting similarities and differences between the DFTRs and NTRs. In the DFTR models, the 8-hydroxyl group of the deazaflavin is H-bonded to Y259 (*Mv*-DFTR) or H234 (*Ma*-DFTR). The corresponding residue in *Ll*-NTR is L240, but in *Ec*-NTR it is also a histidine (H245). Yet, in *Ec*-NTR, this histidine appears to have a different function, making an H-bond to the first oxygen of the NADPH tail (the phosphate oxygen to histidine nitrogen distances vary from 3.2 to 3.4 Å in the four subunits of PDB: 1F6M). Furthermore, in the DFTRs, the hydrophilic moiety of the deazaflavin ring (formed by atoms 1, 2, 3, and 4) is bound almost completely by side chains that are also present in the NTRs. In the NTRs, at the same location as the hydrophilic moiety,

the carboxamide substituent of NADPH's pyridine ring is bound, which has structural similarity [10]. Specifically, at atom position 1, a ring amide hydrogen makes an H-bond to the side chain oxygen of a conserved glutamine (*Ma*-DFTR, Q279; *Mv*-DFTR, Q303; *Ll*-NTR, Q285; *Ec*-NTR, Q294). At position 2, the carboxyl oxygen appears to make H-bonds to the hydroxyl of a conserved tyrosine (*Ma*-DFTR, Y20; *Mv*-DFTR, Y24; *Ll*-NTR, Y23; *Ec*-NTR, Y23) and to the anti-amide hydrogen of a conserved asparagine (*Ma*-DFTR, N48; *Mv*-DFTR, N52; *Ll*-NTR, N51; *Ec*-NTR, N51). At the ring 3 position, the amide is H-bonded to E179 (*Ma*-DFTR)/E195 (*Mv*-DFTR) while in the NTRs, there is a glutamate (E183 in *Ec*-NTR) or glutamine (Q182 in *Lc*-NTR). At position 4 of the isoalloxazine ring, the carboxyl oxygen appears to be H-bonded to an again fully conserved arginine (*Ma*-DFTR, R23; *Mv*-DFTR, R27; *Ll*-NTR, R26; *Ec*-NTR, R26). Further similarities in binding are predicted for the ribityl chain. The first ribityl oxygen (named O2* in F$_{420}$ and O2D in NADPH), makes an H-bond to the syn amide hydrogen of said conserved glutamine (Q279 in *Ma*-DFTR). The second ribityl oxygen makes H-bonds to the backbone amide and carboxyl of the residue N terminus to this glutamine (L278 in *Ma*-DFTR). Further along the tail, the precise contacts for the F$_{420}$ are less clearly defined by the models. It is noteworthy that the number of nearby positively charged residues, lysines and arginines, needed to bind the polyglutamyl tail of F$_{420}$, was similar for the DFTR models and the NTR structures. When all structures were superimposed, within 6 Å of the glutamyl tail, there were six Lys/Arginine residues for *Ma*-DFTR, six for *Mv*-DFTR, five for *Ll*-NTR, and six for *Ec*-NTR.

The models also indicate that, compared to the NTRs, the NADPH binding site is significantly altered to create the F$_{420}$ binding site. In the NTRs, S155 (*L. lactis*) and T156 (*E. coli*) make two H-bonds to

oxygen atoms of the first phosphate from the NADPH tail. This is done via their backbone amide hydrogens and via their side chain hydroxyl hydrogens. In the DFTRs, their replacement by a proline (P151 in *Ma*-DFTR, P167 for *Mv*-DFTR) eliminated these hydrogen bonding interactions (Fig. 6). While F$_{420}$ has a phosphate at the same position in its tail, the preceding ribityl tail is condensed in NADPH while it is not in F$_{420}$, which changes the energetically most favorable position for the phosphate group. Furthermore, the DFTR's proline side chains point in a different direction than the Ser/Thr side chains of the NTRs. This creates space for a feature that is fully absent from NADPH: the benzylic moiety of F$_{420}$. The binding pocket for this moiety is further completed by a methionine (*Ma*-DFTR, M154; *Mv*-DFTR, M170) (Fig. 6B). In the corresponding position in the NTRs, there is glutamate that via its side chain carboxylate oxygen makes an H-bond to the anti-amide proton of the carboxamide substituent of the nicotinamide ring (*Ll*-NTR, E158; *Ec*-NTR, E159) (Fig. 6A). This amide of NADPH is positioned at a different location that the corresponding atom 3 of the deazaflavin ring, which the glutamate would not be able to reach. Thus, it appears that these two replacements, which relinquish interactions that specifically bound the NADPH, are key to providing a more spacious, and more hydrophobic, environment for the benzylic moiety of the deazaflavin cofactor.

Search for DFTRs in Bacteria based on a specific sequence motif

The two archaeal DFTRs reported in this work and the first reported DFTR belong to methanogens. No DFTRs from Bacteria have been reported while many bacteria are F$_{420}$-producers [10]. Having identified two residues that seem to allow F$_{420}$ binding in DFTRs (P167 and M170 in *Mv*-DFTR), we used this sequence fingerprint to check bacterial genomes for potential DFTRs. Together with the two active site cysteines, a sequence motif (CXXC[X]$_{16-18}$PXXM) was defined for performing a PHI-BLAST search. This resulted in the identification of several putative bacterial DFTRs. A gene from the actinomycete *L. tulufanense* was selected for its experimental characterization. This resulted in the expression and purification of a soluble yellow-colored protein, confirming tight binding of a flavin cofactor. The flavoprotein has a T_m of 62 °C as determined by ThermoFAD. To establish whether the *L. tulufanense* DFTR (*Lt*-DFTR) behaves indeed as a thioredoxin reductase and which electron donor it uses, the reductive half-reaction was analyzed

anaerobically employing F$_{420}$H$_2$ and NADPH as electron donors. Employing F$_{420}$H$_2$, *Lt*-DFTR was almost fully reduced in 1 min and spectra could be fitted into a two-step process just like *Ma*-DFTR and *Mv*-DFTR (Fig. 7). The rates for the two kinetic events are 0.17 ± 0.03 s^{-1} and 0.29 ± 0.06 s^{-1}, respectively, while with NADPH no reduction was observed.

Before testing some potential substrates, *Lt*-DFTR was incubated aerobically with 50 μM F$_{420}$H$_2$ to assess whether it can use dioxygen as an electron acceptor. The absorbance change at 400 nm was monitored and revealed a rate of only 0.00032 ± 0.00010 s^{-1}. This shows that *Lt*-DFTR is almost inactive with oxygen, limiting the risk of ROS formation. Next, several typical DFTR substrates, DTNB and *Ma/Mv*-thioredoxins (*Ma/Mv*-Trxs), were tested. With DTNB, the rate of F$_{420}$H$_2$ consumption did not change. However, when using the archaeal thioredoxins, the observed activity was significantly higher, ranging from 0.0015 to 0.0033 s^{-1}. These data confirm that *Lt*-DFTR can indeed act as a F$_{420}$-dependent flavin-containing thioredoxin reductase. To verify that the observed PXXM sequence fingerprint is also shaping the binding pocket for the electron donor, F$_{420}$, in the bacterial enzyme, a structural model of *Lt*-DFTR was prepared. The model was fully compatible with having FAD and F$_{420}$ as ligands, similar to *Ma*-DFTR and *Mv*-DFTR (Fig. S6). Furthermore, the two conserved cysteines are at the analogous position when compared with the archaeal DFTRs, and the proline and methionine are at exactly the same position for forming the binding pocket of part of the F$_{420}$ cofactor (Fig. 6C).

Discussion

The first DFTR was reported a few years ago. Yet, thereafter no other investigations on DFTRs were reported. Many putative DFTR-encoding genes can be identified in sequenced archaeal genomes. This triggered our study that aimed at unraveling the molecular functioning of DFTRs. First, we cloned and expressed two archaeal DFTRs and several thioredoxins from the respective microorganisms. The two DFTRs from *M. aeolicus* and *M. voltae* share low but significant sequence identities (25–35%) with the canonical NTRs. Both proteins could be overexpressed and purification revealed that they are soluble proteins containing a tightly bound FAD cofactor. Both flavoenzymes could be reduced efficiently by F$_{420}$H$_2$ while the use of NADPH was marginal. The relatively high thermostability is another distinct feature of these two DFTRs with apparent melting temperatures of 89 °C and 76 °C for *Ma*-DFTR and *Mv*-DFTR, respectively.
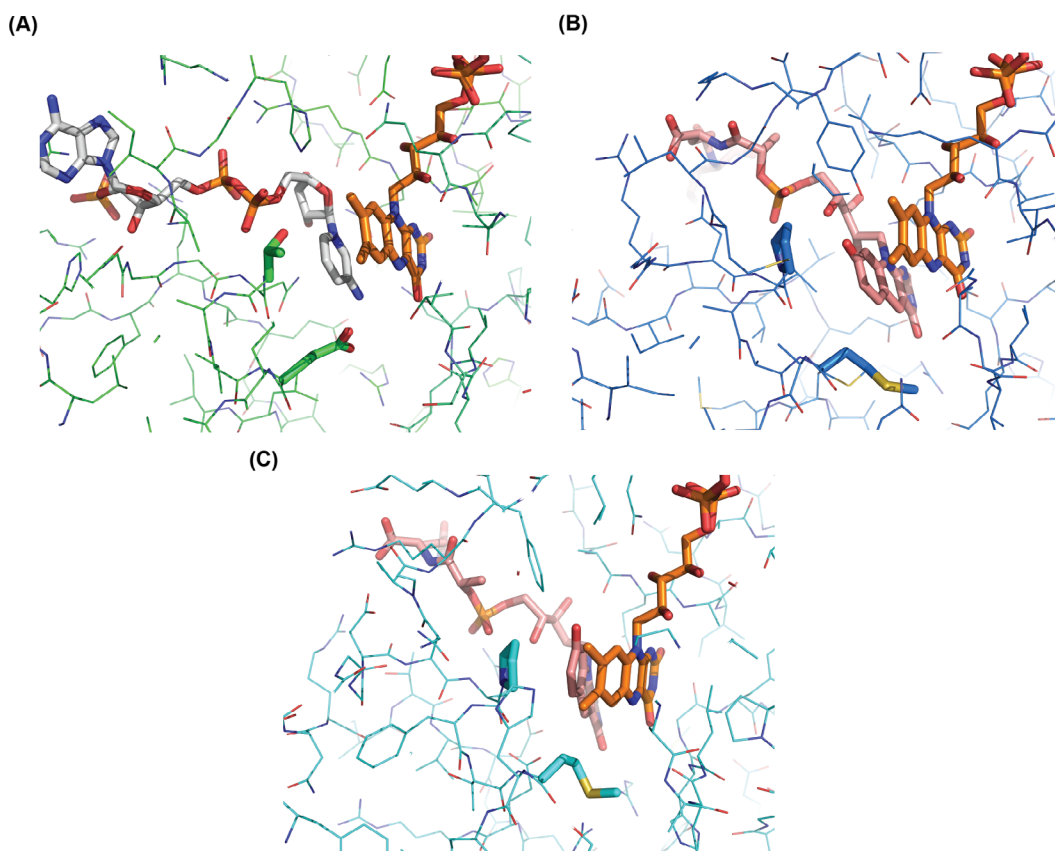
Fig. 6. (A) NADPH binding in *Ec*-NTR (PDB: 1F6M) with the bound NADP derivative in gray sticks. The residues close to the nicotinamide moiety are highlighted (T156 and E159). (B) F$_{420}$ binding in *Mv*-DFTR with the bound F$_{420}$ cofactor in pink sticks. The residues that allow space for the benzyl moiety of the deazaflavin cofactor are highlighted (P167 and M170). (C) F$_{420}$ binding in *Lt*-DFTR with the bound F$_{420}$ cofactor in pink sticks. The residues that allow space for the benzyl moiety of the deazaflavin cofactor are highlighted (P153 and M156). The structures were visualized using PYMOL 2.4.0 (Schrödinger, LLC).

Their putative natural thioredoxin substrates were recombinantly expressed, purified, and found to be bona fide substrates. Except for thioredoxins, the two DFTRs could also accept DTNB as surrogate substrate which is a feature shared by the FAD-containing NTRs. The pre-steady-state kinetic analyses of the wild-type DFTRs and the mutants lacking active-site cysteines revealed that the electron flow is similar to NTRs: from the reduced deazaflavin coenzyme to the FAD cofactor, then to the disulfide redox center in the protein, and finally to the thioredoxin. In the absence of thioredoxin, the reduced DFTRs can slowly react with dioxygen to form superoxide. Yet, the two studied DFTRs are from strictly anaerobic archaea. Hence, such ROS formation would not be a physiologically relevant process.

Upon modeling the F$_{420}$- and FAD-complexed DFTR structures, the residues forming the binding pockets for FAD and F$_{420}$ could be identified. By comparing the structural features with NTRs, the amino acids that could be involved in tuning the coenzyme specificity were identified. Specifically, the specificity for the deazaflavin cofactor could be linked to several substitutions when compared with the NADPH binding pocket in NTRs. The GGGXXA and HRR sequence motifs of NTRs are replaced by GXXXXA and TDK/TEE in the two DFTRs. The analysis of the predicted DFTR structures also highlighted two other residues that differ from NTRs: P151$_{Ma}$/P167$_{Mv}$ and M154$_{Ma}$/M170$_{Mv}$ (Fig. 6). These residues create more space in the active site to accommodate the deazaflavin moiety of the F$_{420}$ molecule. In NTRs, they are substituted by Ser/Thr and Glu which can form H-bonds to NADPH and block binding of F$_{420}$H$_2$. The structural features described above contribute to DFTR preferring F$_{420}$H$_2$ as electron donor while NTRs have a preference for NADPH. Ultimately, our structural analysis resulted in a potential DFTR-
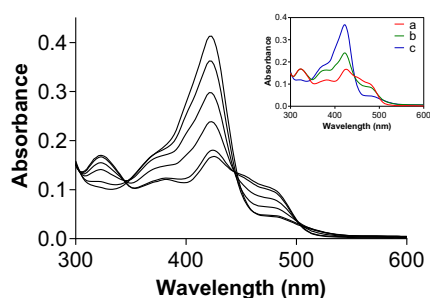
Fig. 7. Reduction of *Lt*-DFTR by F$_{420}$H$_2$. Selected absorbance spectra are shown in the main figure (0.001, 1, 5, 10, 30, and 60 s). The insert shows the deconvoluted spectra using a two-step model (a → b → c), yielding the corresponding fitted k_1 and k_2 rates, respectively. The reaction was conducted anaerobically in a stopped-flow apparatus equipped with a photodiode array module in triplicate. In the reaction, 10 μM *Lt*-DFTR was mixed with 50 μM F$_{420}$H$_2$.

specific sequence fingerprint: (CXXC[X]$_{16–18}$PXXM). Using this sequence motif, more putative DFTRs could be identified in methanogens, but surprisingly also in bacterial genomes. A phylogenetic analysis shows that these enzymes are located in a clade that also contains other thioredoxin reductases that accept alternative electron donors instead of NADPH, such as NADH and ferredoxin (Fig. S7). The occurrence of DFTRs in actinomycetes would be in line with the fact that this group of bacteria are known to produce and utilize the (reduced) F$_{420}$ cofactor. To validate such sequence motif-based identification of novel DFTRs, a putative DFTR-encoding gene identified in the genome of *L. tulufanense* was selected for experimental characterization. The sequence identities between *Lt*-DFTR and known DFTRs/NTRs are only around 20%. *Lt*-DFTR was successfully expressed and purification resulted in a flavin-containing protein. *Lt*-DFTR could be reduced by F$_{420}$H$_2$ with low efficiency but not by NADPH. Also, the activity of *Lt*-DFTR with thioredoxin was confirmed. A structural model of *Lt*-DFTR, containing both redox cofactors, revealed that the active site shares the typical structural features with the archaeal DFTRs, with the conserved proline and methionine forming a binding pocket for the deazaflavin cofactor. Noticeably, *L. tulufanense* is an aerobic bacterium [50]. This suggests that DFTRs are more widespread in nature than what was originally proposed. It demonstrates the plasticity of this family of oxidoreductases in accommodating different electron donors, reducing the tightly bound FAD cofactor. With *L. tulufanense* being only distantly related to archaea, it suggests that affinity toward the deazaflavin cofactor F$_{420}$ as electron donor for thioredoxin

reductases may have evolved multiple times during evolution. Our study suggests that some actinomycetes employ the reduced deazaflavin cofactor for maintaining an intracellular reducing environment. Yet, the exact role of *Lt*-DFTR and closely related enzymes remains to be established.

Materials and methods

Materials

The gene fragments of the three DFTRs and four Trxs were all ordered from Integrated DNA Technologies. *E. coli* NEB 10-β competent cells, ligase, and restriction endonucleases were purchased from New England Biolabs (NEB, Ipswich, MA, USA). All other chemicals and enzymes used in this project were purchased from Sigma-Aldrich (Merck, St. Louis, MO, USA). PfuUltra Hotstart PCR Mastermix was purchased from Agilent Technologies (Santa Clara, CA, USA). F$_{420}$ was purified from *Mycobacterium smegmatis* as previously described [51], and its reduced form, F$_{420}$H$_2$, was produced using an F$_{420}$-dependent glucose-6-phosphate dehydrogenase (Rh-FGD1) and glucose-6-phosphate [52]. F$_{420}$H$_2$ was produced freshly by Rh-FGD1 before use. The reaction mixture contained 200 μM F$_{420}$, 10 mM glucose-6-phosphate, and 1 μM FGD in 50 mM potassium phosphate buffer, pH 8.0, and was incubated at room temperature for 3 h. Then, the mixture was filtered using Amicon Ultra centrifugal filter (10K) (Merck Millipore Ltd., Darmstadt, Germany) at 4 °C to remove the FGD.

Homology searches and phylogenetic analysis

A dataset of biochemically characterized sequences was collected including: six bacterial and archaeal NTRs (NADPH-dependent thioredoxin reductases), two bacterial NTRs reported to use also NADH, one DFTR from archaea, and one bacterial FTR (ferredoxin-dependent thioredoxin reductases). These sequences were employed to perform homology searches using BLASTp, restricting the taxonomy to bacteria and archaea domains, employing non-redundant UniProtKB/SwissProt database. After rounds of manual curation, a dataset was finally obtained including 41 NTR/DFTR/FTR sequences and 15 FNRs (ferredoxin NAD(P)H reductases) to be used as external group in the phylogeny. A multiple sequence alignment was constructed using MAFFT v7 [53] and the presence of the reported motifs [33] was analyzed. A phylogeny was inferred using RAXML v8.2.10 [54], with 500 bootstraps (BS). BS values were transformed to transfer bootstrap expectation values in BOOSTER [55]. FIGTREE 1.4.2 (http://tree.bio.ed.ac.uk/software/figtree/) was used to visualize the tree.

Ma-DFRT (UNIPROT: A6UV27) and *Mv*-DFTR (UNIPROT: D7DT65) were selected on the basis of their medium sequence identity ($\approx$ 50%) to the previously reported *Mj*-DFTR (UNIPROT: Q58931). The corresponding Trxs were found by homology searches using the Trx1 from *E. coli* (UNIPROT: P0AA25) as query in either *M. voltae* or *M. aeolicus*.

Expression

The DFTR genes were cloned into a pBAD vector with N-terminal His6x-SUMO-tag while the four Trx genes were cloned into a pBAD vector with N-terminal His6x-tag. The Golden Gate Cloning mixture contained the gene fragments, vectors, BsaI restriction enzyme, T4 ligase, ligation buffer, and Milli-Q water. The incubation temperature alternated between 37 °C for 5 min and 16 °C for 10 min for 30 cycles, then was set to 55 °C for 10 min, and finally to 65 °C for 20 min to inactivate the enzymes. Then, 3.5 µL of constructed plasmids was added into 100 µL of chemically competent *E. coli* NEB 10-beta cells. After transformation, the plates were incubated at 37 °C overnight. Two to three colonies of each protein were selected to grow in a medium overnight. The plasmids were extracted using QIAGEN kit (QIAGEN, Hilden, Germany) for miniprep from harvested cells and sent to sequence.

Site-directed mutagenesis

Site-directed mutagenesis was carried out by using the pBAD-His6x-SUMO-DFTR plasmids as templates. The primers used are listed in Table S2. The 25 -µL PCR reaction mixtures contained 20–30 ng template, 0.2 µM forward and reverse primers, and 12.5-µL PfuUltra II Hotstart PCR Master Mix, which include optimized PCR reaction buffer, magnesium, and dNTPs. The mixtures were subjected to the following PCR conditions: 95 °C for 3 min, 30 cycles of 95 °C for 30 s, 60 °C for 30 s and 72 °C for 3 min, and a final extension at 72 °C for 5 min. The PCR products were digested by DpnI at 37 °C to remove the parental templates, after which the reaction mixtures were transformed into chemically competent *E. coli* NEB 10-beta cells. Two or three colonies were picked for each mutant and the mutations were verified by sequencing.

Enzyme purification

All studied DFTRs and Trxs were purified by affinity chromatography. The recombinant strains were grown at 37 °C in 200-mL TB medium containing 50 µg·mL^{-1} ampicillin. L-Arabinose was added when the OD$_{600}$ was 0.6–0.8, with a final concentration of 0.02% w/v. Then, the culture was incubated at 24 °C for 20 h. Cells were harvested by centrifugation at 4 °C, 6000 *g* for 20 min. The cells were resuspended in 50-mM potassium phosphate buffer, pH 8.0, containing 1 µg·mL^{-1} DNase, 1 mM phenylmethylsulphonyl fluoride, 1 mg·mL^{-1} lysozyme, and 1 mM MgCl$_2$. The cells were disrupted by sonication and spun down at 4 °C, 12 000 *g* for 60 min. The supernatant was loaded onto the Ni-Sepharose HP column (GE Healthcare Lifesciences) which had been equilibrated with 50 mM potassium phosphate buffer, pH 8.0. The column was incubated at 4 °C for 1 h. Then, the supernatant was eluted and the column was washed with 10 column volumes (CV) of 50-mM potassium phosphate buffer. Thereafter, another washing step was performed by adding 10 CVs of 50-mM potassium phosphate buffer containing 10-mM imidazole. Finally, the protein was eluted using 50-mM potassium phosphate buffer with 500-mM imidazole. The fractions containing the target proteins were collected and desalted by using a HiPrep 26/10 desalting column (GE Healthcare Lifesciences) with 50-mM potassium phosphate buffer. Desalted protein aliquots were then flash-frozen in liquid nitrogen and stored at −70 °C. The concentration of *Ma*-DFTR and *Mv*-DFTR was determined by using a molar absorption coefficient of 12 440 and 13 100 M^{-1}·cm^{-1} at 450 nm, respectively, while that of the four thioredoxins was determined using the Bradford assay.

The F$_{420}$-dependent glucose-6-phosphate dehydrogenase from *Rhodococcus jostii* RHA1 (Rh-FGD1) was expressed and purified as previously described [52]. The protein concentration was determined using the Bradford assay.

Size exclusion chromatography and dynamic light scattering analysis

For SEC and DLS experiments, the 6xHis-SUMO-tag was removed from *Ma*-DFTR and *Mv*-DFTR via SUMO-protease digestion. SEC was performed at 7 °C using a Superdex200 10/300 column (Cytiva), equilibrated with 20 mM TRIS buffer, pH 7.5, containing 150 mM NaCl. The absorbance was monitored at 254, 280, and 385 nm (Fig. S2). For both proteins, *Ma*-DFTR and *Mv*-DFTR, the major peaks (eluting at 14.1–14.4 mL) were collected and concentrated to $\sim$ 12 mg·mL^{-1} using an Amicon Ultra centrifugal filter unit (Merck Millipore Ltd.) with 10 kDa cut-off. *Ma*-DFTR and *Mv*-DFTR samples were also analyzed by DLS on a DynaPro NanoStar instrument at 21 °C (Wyatt Technology, Santa Barbara, CA, USA) using samples of 10 mg·mL^{-1} protein in 25-mM TRIS–HCl, pH 7.5, and 150 mM NaCl.

Insulin reduction assay

An insulin reduction assay was performed under anaerobic environment as previously described [33,56,57]. In this experiment, the reaction mixture contained 30-µM bovine insulin, 100 µM F$_{420}$H$_2$, 10 µM Trx, 0.1 µM DFTR, and

2 mM EDTA in 100-mM HEPES buffer, pH 7.4. The reactions were carried out in an SX20 stopped-flow spectrometer equipped with a diode-array detector (Applied Photophysics, Surrey, UK). Before experiments, the stopped-flow system was washed with anaerobic buffer. All reaction components were flushed by nitrogen and mixed with glucose oxidase and glucose to remove dissolved oxygen. During the reaction, absorbance changes were monitored using the diode-array detector. All measurements were performed at 25 °C in triplicate.

pH optimization

The activities of the archaeal DFTRs were determined at pH values ranging from 4.0 to 9.0. Three different buffers, TRIS–HCl, potassium phosphate, and acetic acid–sodium acetate buffer, were used to cover the pH range. The reaction mixtures (total volume 100 μL), containing 100 nM *Ma*-DFTR/25 nM *Mv*-DFTR, 30 μM F$_{420}$H$_2$, 10 μM *Ma*-Trx2/*Mv*-Trx1, and 1 mM glutathione, were used anaerobically in a SX20 stopped-flow apparatus at 25 °C. Consumption of F$_{420}$H$_2$ was monitored at 400 nm by a photomultiplier tube detector. All measurements were performed in triplicate.

Temperature optimization

To determine the effect of temperature, the activities of the two archaeal enzymes were measured at every 5 °C from 20 °C to 50 °C. The range chosen here is limited by temperature range of stopped-flow apparatus. The reactions contained 100 nM *Ma*-DFTR/25 nM *Mv*-DFTR, 50 μM F$_{420}$H$_2$, 5 μM *Ma*-Trx2/*Mv*-Trx1, and 1 mM glutathione in 50-mM potassium phosphate buffer, pH 8.0. All measurements were monitored at 400 nm by a photomultiplier tube detector in triplicate.

Thermostability

The ThermoFAD [36] and Thermofluor [37] methods were used to determine T_m values. The enzyme samples (20 μL) containing 10-μM purified protein in 50-mM potassium phosphate buffer, pH 8.0, were heated up from 25 °C to 90 °C in an RT-PCR thermocycler and held for 10 s when the temperature increased by each 0.5 °C. Intensity of fluorescence was measured after each holding time. The maxima of the first derivative of the observed fluorescence were taken as the apparent melting temperatures. All measurements were in triplicate.

Steady-state kinetics

The kinetics of the two archaeal DFTRs toward F$_{420}$H$_2$, NADPH, and thioredoxins were determined by using a

stopped-flow apparatus under anaerobic conditions at 25 °C. The 100-μL reaction mixtures contained 2 mM EDTA, 100 nM *Ma*-DFTR or 25 nM *Mv*-DFTR, an electron donor and a substrate in 50-mM potassium phosphate buffer, pH 8.0. 1.0 mM 5,5′-dithiobis(2-nitrobenzoic acid) (DTNB) was used as the substrate for the kinetics measurements of F$_{420}$H$_2$ and NADPH. 60 μM F$_{420}$H$_2$ was used as an electron donor for the kinetics measurements of thioredoxins. The concentrations of thioredoxins, F$_{420}$H$_2$, and NADPH varied. The reactions were initiated by mixing in the stopped-flow and were monitored by absorbance detection at 400 nm (formation of F$_{420}$) or 412 nm (formation of 5-thio-2-nitrobenzoic acid, TNB, from DTNB). The rate was calculated by using extinction coefficients of 25.7 mM^{-1}·cm^{-1} (F$_{420}$ at 400 nm) and 14.15 mM^{-1}·cm^{-1} (TNB at 412 nm). For measurement in which both DTNB and F$_{420}$H$_2$ were present, the increase in absorbance at 400 nm was measured to monitor the formation of both F$_{420}$ and TNB. For this, a combined extinction coefficient of 49.5 mM^{-1}·cm^{-1} ($\varepsilon_{F420,400\ nm} + 2 \times \varepsilon_{TNB,400\ nm} = 25.7 + 2 \times 11.9$) was used. All reactions were run in triplicate. All data were fitted by using GRAPHPAD PRISM (Dotmatics, Boston, MA, USA) using the Michaelis–Menten or substrate inhibition equations.

Reductive half-reaction

The reductive half-reactions of the DFTRs were conducted anaerobically at 10 °C by using a SX20 stopped-flow apparatus in triplicate. Both FAD reduction and F$_{420}$ formation were monitored by a photodiode array module at full wavelength. The reaction mixtures contained DFTRs (10 or 5 μM) and F$_{420}$H$_2$ or NADPH with varied concentrations in 50 mM potassium phosphate buffer, pH 8.0. The data were analyzed by Pro-kineticist (Applied Photophysics Ltd.).

Uncoupling activity

To determine the effect of the presence of oxygen, peroxidase and cytochrome *c* were used to detect the possible ROS formed in the process. For hydrogen peroxide, HRP was used to catalyze the reaction between 3,5-dichloro-2-hydroxy-benzenesulfonic acid (DCHBS) and hydrogen peroxide. The product can further react with 4-aminoantipyrine (AAP) to form a red dye, which has a maximum absorbance of 515 nm ($\varepsilon_{515\ nm} = 27$ mM^{-1}·cm^{-1}). The reaction mixtures, containing 1.0 μM DFTR, 1.0 mM DCHBS, 1.0 mM AAP, 0.008 U·μL^{-1} HRP, and 50 μM F$_{420}$H$_2$ in 50 mM potassium phosphate buffer, pH 8.0, were monitored for absorbance increase in a microplate photometer at 25 °C. All measurements were performed in triplicate.

For superoxide, the cytochrome *c* reduction assay was applied. Oxidized cytochrome *c* can be reduced by superoxide and it can be monitored through formation of an

absorption peak at λ_{max} of 550 nm ($\varepsilon_{550\ nm} = 28\ mM^{-1}\cdot cm^{-1}$). The reaction mixture contained 1.0 μM DFTR, 50 μM F$_{420}$H$_2$, and 50 μM cytochrome *c* in 50-mM potassium phosphate buffer, pH 8.0 (25 °C). Super-oxide can spontaneously form hydrogen peroxide, which can oxidize cytochrome *c* (Fe^{2+}) back to cytochrome *c* (Fe^{3+}). To prevent such an influence of hydrogen peroxide, reactions with 50 μg·mL^{-1} catalase were performed as controls. All measurements were done in triplicate.

Structure predictions and modeling

The three-dimensional structures of *Ma*-DFTR and *Mv*-DFTR were predicted using AlphaFold2 [42]. *Ma*-DFTR was modeled with CASP14 settings and *Mv*-DFTR with the (faster) full dbs settings. AlphaFold2 modeled the structures as monomers, which were converted to the physiological dimers by duplication and superimposition on a crystal structure of an NTR (PDB: 5MH4, NTR from *L. lactis* [49]). The FAD binding orientation was obtained by superimposing the modeled structures to the NTR from *L. lactis*. Prior to manual docking of F$_{420}$, the natural binding modes of F$_{420}$ to deazaflavoproteins were explored to become familiar with the hydrogen bonding patterns of natural F$_{420}$-protein complexes. The PDB was searched for high-resolution (< 2.0 Å) protein structures with a F$_{420}$ bound. A total of five structures were found and inspected [44–48]. Automated dockings were carried out as well with previously established protocols [58,59], but those failed to produce catalytically productive poses; no poses were found with a short distance (< 4.0 Å) between the redox-active carbon (C5) and nitrogen (N5) atoms of the F$_{420}$ and FAD cofactors. Manual docking of F$_{420}$ to the *Ma*-DFTR and *Mv*-DFTR predicted structural models was started by visualizing the binding cavity on top of the riboflavin moiety of the FAD cofactor with molecular surface [60]. Subsequently, a collection of all the F$_{420}$ conformations available from PDB X-ray structures (found by looking for the F$_{420}$ ligand on www.rcsb.org) was collected and used for docking. The deazaflavin head group was manually inserted in the binding pocket such that a minimal number of unsatisfied H-bond donors and acceptors was generated. Subsequently, a conformation of the F$_{420}$ was picked that did not display steric clashes with the modeled protein (it originated from structure PDB: 1Z69 [61]). Energy minimizations were performed using the YASARA force field, which is a statistical-learning-based force field specifically developed for improving homology models [62]. Initially, an energy minimization was performed in which the protein was frozen (with the exception of one methionine (M154 in *Ma*-DFTR and M170 in *Mv*-DFTR) which during Alpha-Fold2 modeling had adopted a rotamer position that gave clashes with the isoalloxazine ring). Subsequently, in an additional energy minimization step, all protein side chains

and the bound F$_{420}$H$_2$ and FAD were allowed to move. The resulting structures were the final models.

For *Lt*-DFTR, YASARA models were generated as well, using the AlphaFold predicted *Ma*-DFTR and *Mv*-DFTR as template structures [62]. AlphaFold modeling of *Lt*-DFTR resulted in the FO structure, which did not allow to model binding of the F$_{420}$ cofactor. During the initial modeling, the automatically generated sequence alignments appeared to cause a frame-shift error that moved the proline and methionines of the sequence motif by one position toward the C terminus, causing them to point away from the F$_{420}$ molecule as they were located in an α-helix. Therefore, the sequence alignment for the structural modeling was provided using T-COFFEE [63], using the *Ma*-DFTR and *Mv*-DFTR templates and the *Lt*-DFTR sequence. This automatically generated alignment resulted in the final model for *Lt*-DFTR, which included the F$_{420}$ and flavin cofactors from the template structures, and is included in the Supporting Information.

Conflict of interest

The authors declare no conflict of interest.

Author contributions

All authors listed contributed experimental/computational work and/or data analysis. MWF conceived the project. MWF and GY planned the experiments. HJW generated the computationally predicted structures and performed docking of the cofactors. HJR performed size exclusion chromatography, dynamic light scattering, and crystallization experiments. MLM performed homology searches for new DFTRs and phylogenetic analysis. GY performed all other experiments. GY wrote the main part of the manuscript, while HJW, HJR, and MLM wrote the results and methods parts of structure prediction, SEC/DLS experiments, and homology searches, respectively. MWF edited and revised the manuscript.

Peer review

The peer review history for this article is available at https://www.webofscience.com/api/gateway/wos/peer-review/10.1111/febs.16896.

Data availability statement

Additional data supporting the results of this study can be found in the [Supporting Information](#) or are available from the corresponding authors upon reasonable request.

References

1 Cheeseman P, Toms-Wood A & Wolfe RS (1972) Isolation and properties of a fluorescent compound, factor$_{420}$, from *Methanobacterium* strain M.o.H. *J Bacteriol* **112**, 527–531.

2 Eirich LD, Vogels GD & Wolfe RS (1979) Distribution of coenzyme F$_{420}$ and properties of its hydrolytic fragments. *J Bacteriol* **140**, 20–27.

3 van Beelen P, Dijkstra AC & Vogels GD (1983) Quantitation of coenzyme F$_{420}$ in methanogenic sludge by the use of reversed-phase high-performance liquid chromatography and a fluorescence detector. *Eur J Appl Microbiol Biotechnol* **18**, 67–69.

4 Dolfing J & Mulder J (1985) Comparison of methane production rate and coenzyme F$_{420}$ content of methanogenic consortia in anaerobic granular sludge. *Appl Environ Microbiol* **49**, 1142–1145.

5 Eker APM, Pol A, van der Meyden P & Vogels GD (1980) Purification and properties of 8-hydroxy-5-deazaflavin derivatives from *Streptomyces griseus*. *FEMS Microbiol Lett* **8**, 161–165.

6 Daniels L, Bakhiet N & Harmon K (1985) Widespread distribution of a 5-deazaflavin cofactor in actinomyces and related bacteria. *Syst Appl Microbiol* **6**, 12–17.

7 Kuo MT, Yurek DA, Coats JH & Li GP (1988) Isolation and identification of 7,8-didemethyl-8-hydroxy-5-deazariboflavin, an unusual cosynthetic factor in streptomycetes, from *Streptomyces lincolnensis*. *J Antibiot (Tokyo)* **7**, 475–478.

8 Ebert S, Rieger P & Knackmuss H (1999) Function of coenzyme F$_{420}$ in aerobic catabolism of 2,4,6-trinitrophenol and 2,4-dinitrophenol by *Nocardioides simplex* FJ2-1A. *J Bacteriol* **181**, 2669–2674.

9 Purwantini E, Gillis TP & Daniels L (1997) Presence of F$_{420}$-dependent glucose-6-phosphate dehydrogenase in *Mycobacterium* and *Nocardia* species, but absence from *Streptomyces* and *Corynebacterium* species and methanogenic Archaea. *FEMS Microbiol Lett* **146**, 129–134.

10 Grinter R & Greening C (2021) Cofactor F$_{420}$: an expanded view of its distribution, biosynthesis and roles in bacteria and archaea. *FEMS Microbiol Rev* **45**, fuab021.

11 Ney B, Ahmed FH, Carere CR, Biswas A, Warden AC, Morales SE, Pandey G, Watt SJ, Oakeshott JG, Taylor MC *et al.* (2017) The methanogenic redox cofactor F$_{420}$ is widely synthesized by aerobic soil bacteria. *ISME J* **11**, 125–137.

12 Braga D, Hasan M, Kröber T, Last D & Lackner G (2020) Redox coenzyme F$_{420}$ biosynthesis in Thermomicrobia involves reduction by stand-alone nitroreductase superfamily enzymes. *Appl Environ Microbiol* **86**, e00457-20.

13 Braga D, Last D, Hasan M, Guo H, Leichnitz D, Uzum Z, Richter I, Schalk F, Beemelmanns C, Hertweck C *et al.* (2019) Metabolic pathway rerouting in *Paraburkholderia rhizoxinica* evolved long-overlooked derivatives of coenzyme F$_{420}$. *ACS Chem Biol* **14**, 2088–2094.

14 Tzeng SF, Bryant MP & Wolfe RS (1975) Factor 420-dependent pyridine nucleotide-linked formate metabolism of *Methanobacterium ruminantium*. *J Bacteriol* **121**, 192–196.

15 Hagemeier CH, Shima S, Thauer RK, Bourenkov G, Bartunik HD & Ermler U (2003) Coenzyme F$_{420}$-dependent methylenetetrahydromethanopterin dehydrogenase (Mtd) from *Methanopyrus kandleri*: a methanogenic enzyme with an unusual quarternary structure. *J Mol Biol* **332**, 1047–1057.

16 Aufhammer SW, Warkentin E, Berk H, Shima S, Thauer RK & Ermler U (2004) Coenzyme binding in F$_{420}$-dependent secondary alcohol dehydrogenase, a member of the bacterial luciferase family. *Structure* **12**, 361–370.

17 Vitt S, Ma K, Warkentin E, Moll J, Pierik AJ, Shima S & Ermler U (2014) The F$_{420}$-reducing [NiFe]-hydrogenase complex from *Methanothermobacter marburgensis*, the first X-ray structure of a group 3 family member. *J Mol Biol* **426**, 2813–2826.

18 Schauert NL & Ferry JG (1986) Composition of the coenzyme F$_{420}$-dependent formate dehydrogenase from *Methanobacterium formicicum*. *J Bacteriol* **165**, 405–411.

19 Purwantini E & Mukhopadhyay B (2009) Conversion of NO$_2$ to NO by reduced coenzyme F$_{420}$ protects mycobacteria from nitrosative damage. *Proc Natl Acad Sci USA* **106**, 6333–6338.

20 Gurumurthy M, Rao M, Mukherjee T, Rao SPS, Boshoff HI, Dick T, Barry CE 3rd & Manjunatha UH (2013) A novel F$_{420}$-dependent anti-oxidant mechanism protects *Mycobacterium tuberculosis* against oxidative stress and bactericidal agents. *Mol Microbiol* **87**, 744–755.

21 Hasan MR, Rahman M, Jaques S, Purwantini E & Daniels L (2010) Glucose 6-phosphate accumulation in mycobacteria. Implications for a novel F$_{420}$-dependent anti-oxidant defense system. *J Biol Chem* **285**, 19135–19144.

22 Stover CK, Warrrener P, VanDevanter DR, Sherman DR, Arain TM, Langhorne MH, Anderson SW, Towel JA, Yuan Y, McMurray DN *et al.* (2000) A small-

molecule nitroimidazopyran drug candidate for the treatment of tuberculosis. *Nature* **405**, 962–966.

23 Jiraskova P, Gazak R, Kamenik Z, Steiningerova L, Najmanova L, Kadlcik S, Novotna J, Kuzma M & Janata J (2016) New concept of the biosynthesis of 4-alkyl-L-proline precursors of lincomycin, hormaomycin & pyrrolobenzodiazepines: could a γ-glutamyltransferase cleave the C-C bond? *Front Microbiol* **7**, 276.

24 Janata J, Kamenik Z, Gazak R, Kadlcik S & Najmanova L (2018) Biosynthesis and incorporation of an alkylproline-derivative (APD) precursor into complex natural products. *Nat Prod Rep* **35**, 257–289.

25 Steiningerova L, Kamenik Z, Gazak R, Kadlcik S, Bashiri G, Man P, Kuzma M, Pavlikova M & Janata J (2020) Different reaction specificities of F$_{420}$H$_2$-dependent reductases facilitate pyrrolobenzodiazepines and lincomycin to fit their biological targets. *J Am Chem Soc* **142**, 3440–3448.

26 Ichikawa H, Bashiri G & Kelly WL (2018) Biosynthesis of the thiopeptins and identification of an F$_{420}$H$_2$-dependent dehydropiperidine reductase. *J Am Chem Soc* **140**, 10749–10756.

27 Wang P, Bashiri G, Gao X, Sawaya MR & Tang Y (2013) Uncovering the enzymes that catalyze the final steps in oxytetracycline biosynthesis. *J Am Chem Soc* **135**, 7138–7141.

28 Greening C, Ahmed FH, Mohamed AE, Lee BM, Pandey G, Warden AC, Scott C, Oakeshott JG, Taylor MC & Jackson CJ (2016) Physiology, biochemistry & applications of F$_{420}$- and Fo-dependent redox reactions. *Microbiol Mol Biol Rev* **80**, 451–493.

29 Jacobson F & Walsh C (1984) Properties of 7,8-didemethyl-8-hydroxy-5-deazaflavins relevant to redox coenzyme function in methanogen metabolism. *Biochemistry* **23**, 979–988.

30 Edmondson DE, Barman B & Tollin G (1972) On the importance of the N-5 position in flavin coenzymes. Properties of free and protein-bound 5-deaza analogs. *Biochemistry* **11**, 1133–1138.

31 Xia K, Shen G & Zhu X (2015) Thermodynamics of various F$_{420}$ coenzyme models as sources of electrons, hydride ions, hydrogen atoms and protons in acetonitrile. *Org Biomol Chem* **13**, 6255–6268.

32 Shah M, Antoney J, Kang SW, Warden AC, Hartley CJ, Nazem-Bokaee H, Jackson CJ & Scott C (2019) Cofactor F$_{420}$-dependent enzymes: an under-explored resource for asymmetric redox biocatalysis. *Catalysts* **9**, 868.

33 Susanti D, Loganathan U & Mukhopadhyay B (2016) A novel F$_{420}$-dependent thioredoxin reductase gated by low potential FAD: a tool for redox regulation in an anaerobe. *J Biol Chem* **291**, 23084–23100.

34 Arnér ESJ & Holmgren A (2000) Physiological functions of thioredoxin and thioredoxin reductase. *Eur J Biochem* **267**, 6102–6109.

35 Gromer S, Urig S & Becker K (2004) The thioredoxin system – from science to clinic. *Med Res Rev* **24**, 40–89.

36 Forneris F, Orru R, Bonivento D, Chiarelli LR & Mattevi A (2009) ThermoFAD, a Thermofluor®-adapted flavin ad hoc detection system for protein folding and ligand binding. *FEBS J* **276**, 2833–2840.

37 Pantoliano MW, Petrella EC, Kwasnoski JD, Lobanov VS, Myslik J, Graf E, Carver T, Asel E, Springer BA, Lane P *et al.* (2001) High-density miniaturized thermal shift assays as a general strategy for drug discovery. *J Biomol Screen* **6**, 429–440.

38 Sheng Y, Abreu IA, Cabelli DE, Maroney MJ, Miller AF, Teixeira M & Valentine JS (2014) Superoxide dismutases and superoxide reductases. *Chem Rev* **114**, 3854–3918.

39 McCarver AC & Lessner DJ (2014) Molecular characterization of the thioredoxin system from *Methanosarcina acetivorans*. *FEBS J* **281**, 4598–4611.

40 Yang X & Ma K (2010) Characterization of a thioredoxin-thioredoxin reductase system from the hyperthermophilic bacterium *Thermotoga maritima*. *J Bacteriol* **192**, 1370–1376.

41 Jeon S & Ishikawa K (2002) Identification and characterization of thioredoxin and thioredoxin reductase from *Aeropyrum pernix* K1. *Eur J Biochem* **269**, 5423–5430.

42 Jumper J, Evans R, Pritzel A, Green T, Figurnov M, Ronneberger O, Tunyasuvunakool K, Bates R, Žídek A, Potapenko A *et al.* (2021) Highly accurate protein structure prediction with AlphaFold. *Nature* **596**, 583–589.

43 Lennon BW, Williams CH Jr & Ludwig ML (2000) Twists in catalysis: alternating conformations of *Escherichia coli* thioredoxin reductase. *Science* **289**, 1190–1194.

44 Ahmed FH, Carr PD, Lee BM, Afriat-Jurnou L, Mohamed AE, Hong NS, Flanagan J, Taylor MC, Greening C & Jackson CJ (2015) Sequence-structure-function classification of a catalytically diverse oxidoreductase superfamily in mycobacteria. *J Mol Biol* **427**, 3554–3571.

45 Cellitti SE, Shaffer J, Jones DH, Mukherjee T, Gurumurthy M, Bursulaya B, Boshoff HI, Choi I, Nayyar A, Lee YS *et al.* (2012) Structure of Ddn, the deazaflavin-dependent nitroreductase from *Mycobacterium tuberculosis* involved in bioreductive activation of PA-824. *Structure* **20**, 101–112.

46 Ceh K, Demmer U, Warkentin E, Moll J, Thauer RK, Shima S & Ermler U (2009) Structural basis of the hydride transfer mechanism in F$_{420}$-dependent methylenetetrahydromethanopterin dehydrogenase. *Biochemistry* **48**, 10098–10105.

47 Bashiri G, Squire CJ, Moreland NJ & Baker EN (2008) Crystal structures of F$_{420}$-dependent glucose-6-

phosphate dehydrogenase FGD1 involved in the activation of the anti-tuberculosis drug candidate PA-824 reveal the basis of coenzyme and substrate binding. *J Biol Chem* **283**, 17531–17541.

48 Warkentin E, Mamat B, Sordel-Klippert M, Wicke M, Thauer RK, Iwata M, Iwata S, Ermler U & Shima S (2001) Structures of F$_{420}$H$_2$:NADP$^+$ oxidoreductase with and without its substrates bound. *EMBO J* **20**, 6561–6569.

49 Skjoldager N, Bang MB, Rykær M, Björnberg O, Davies MJ, Svensson B, Harris P & Hägglund P (2017) The structure of *Lactococcus lactis* thioredoxin reductase reveals molecular features of photo-oxidative damage. *Sci Rep* **7**, 46282.

50 Xia Z, Guan T, Ruan J, Huang Y & Zhang L (2013) *Longimycelium tulufanense* gen. nov., sp. nov., a filamentous actinomycete of the family Pseudonocardiaceae. *Int J Syst Evol Microbiol* **63**, 2813–2818.

51 Isabelle D, Simpson DR & Daniels L (2002) Large-scale production of coenzyme F$_{420}$-5,6 by using *Mycobacterium smegmatis*. *Appl Environ Microbiol* **68**, 5750–5755.

52 Nguyen QT, Trinco G, Binda C, Mattevi A & Fraaije MW (2017) Discovery and characterization of an F$_{420}$-dependent glucose-6-phosphate dehydrogenase (Rh-FGD1) from *Rhodococcus jostii* RHA1. *Appl Microbiol Biotechnol* **101**, 2831–2842.

53 Katoh K, Rozewicki J & Yamada KD (2018) MAFFT online service: multiple sequence alignment, interactive sequence choice and visualization. *Brief Bioinform* **20**, 1160–1166.

54 Stamatakis A (2014) RAxML version 8: a tool for phylogenetic analysis and post-analysis of large phylogenies. *Bioinformatics* **30**, 1312–1313.

55 Lemoine F, Domelevo Entfellner J, Wilkinson E, Correia D, Dávila Felipe M, de Oliveira T & Gascuel O (2018) Renewing Felsenstein's phylogenetic bootstrap in the era of big data. *Nature* **556**, 452–456.

56 Holmgren A (1977) Bovine thioredoxin system. Purification of thioredoxin reductase from calf liver and thymus and studies of its function in disulfide reduction. *J Biol Chem* **252**, 4600–4606.

57 Susanti D, Wong JH, Vensel WH, Loganathana U, DeSantis R, Schmitz RA, Balsera M, Buchanan BB & Mukhopadhyay B (2014) Thioredoxin targets fundamental processes in a methane-producing archaeon, *Methanocaldococcus jannaschii*. *Proc Natl Acad Sci USA* **111**, 2608–2613.

58 Morris GM, Huey R, Lindstrom W, Sanner MF, Belew RK, Goodsell DS & Olson AJ (2009) AutoDock4 and AutoDockTools4: automated docking with selective receptor flexibility. *J Comput Chem* **30**, 2785–2791.

59 Wijma HJ, Marrink SJ & Janssen DB (2014) Computationally efficient and accurate enantioselectivity modeling by clusters of molecular dynamics simulations. *J Chem Inf Model* **54**, 2079–2092.

60 Krieger E & Vriend G (2014) YASARA view – molecular graphics for all devices – from smartphones to workstations. *Bioinformatics* **30**, 2981–2982.

61 Aufhammer SW, Warkentin E, Ermler U, Hagemeier CH, Thauer RK & Shima S (2005) Crystal structure of methylenetetrahydromethanopterin reductase (Mer) in complex with coenzyme F$_{420}$: architecture of the F$_{420}$/FMN binding site of enzymes within the nonprolyl cis-peptide containing bacterial luciferase family. *Protein Sci* **14**, 1840–1849.

62 Krieger E, Joo K, Lee J, Lee J, Raman S, Thompson J, Tyka M, Baker D & Karplus K (2009) Improving physical realism, stereochemistry & side-chain accuracy in homology modeling: four approaches that performed well in CASP8. *Proteins* **77**, 114–122.

63 Notredame C, Higgins DG & Heringa J (2000) T-coffee: a novel method for fast and accurate multiple sequence alignment. *J Mol Biol* **302**, 205–217.

64 Navarro JA, Gleason FK, Cusanovich MA, Fuchs JA, Meyer TE & Tollin G (1991) Kinetics of electron transfer from thioredoxin reductase to thioredoxin. *Biochemistry* **30**, 2192–2195.

Supporting information

Additional supporting information may be found online in the Supporting Information section at the end of the article.

Fig. S1. SDS/PAGE analysis of purified DFTRs and Trxs.
Fig. S2. UV–Vis Absorbance spectra of Ma-DFTR, Mv-DFTR, and Lt-DFTR.
Fig. S3. Thermostabilities of DFTRs.
Fig. S4. Activities of Ma-DFTR and Mv-DFTR toward 50 μM F$_{420}$H$_2$ and 5 μM thioredoxin at 20–50 °C.
Fig. S5. Reductive half-reaction of Ma-DFTR.
Fig. S6. AlphaFold2-predicted model of DFTR monomers with docked cofactors.
Fig. S7. Maximum Likelihood tree of thioredoxin reductases using different hydride donors.
Table S1. Reduction rates with F$_{420}$H$_2$ as an electron donor.
Table S2. Quick change primers for site-directed mutagenesis of Ma-DFTR and Mv-DFTR.